ACS APPLIED MATERIALS & INTERFACES

Research Article

Cite This: ACS Appl. Mater. Interfaces 2019, 11, 12986−12992

www.acsami.org

Hofmann Metal−Organic Framework Monolayer Nanosheets as an Axial Coordination Platform for Biosensing

Bernardino J. Córdova Wong,[†] Di-ming Xu,[‡] Song-Song Bao,[‡] Li-Min Zheng,*[,‡] and Jianping Lei*[,†]

[†]State Key Laboratory of Analytical Chemistry for Life Science, School of Chemistry and Chemical Engineering, and [‡]State Key Laboratory of Coordination Chemistry, School of Chemistry and Chemical Engineering, Nanjing University, Nanjing 210023, P. R. China

Supporting Information

ABSTRACT: Two-dimensional (2D) nanomaterials are remarkably attractive platform candidates for signal transduction through fluorescence resonance energy transfer or photo-induced electron-transfer pathway. In this work, a 2D Hofmann metal organic framework (hMOF) monolayer nanosheet was developed as an axial coordination platform for DNA detection via a ligand-to-metal charge-transfer quenching mechanism. Through modulating the position of phosphonate groups of rigid ligands, a layer-structured hMOF was synthesized. The single crystals showed that the adjacent layers were linked via hydrogen bonds between diethyl 4-pyridylphosphonate and the solvent. Furthermore, the 2D hMOF monolayer nanosheets were obtained easily via a top−down method. More significantly, the quenching mechanism was identified as an axial coordination between the open Fe^{2+} sites of hMOF nanosheets and fluorophores with 91% quenching efficiency, constituting an excellent signal transduction strategy. The smart use of hMOF monolayer nanosheets as an axial coordination platform could lead to promising applications in signal switching or/and sensing devices.

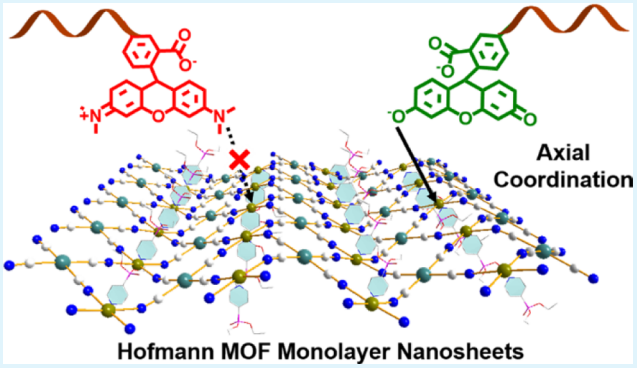

KEYWORDS: *Hofmann metal−organic framework, monolayer, axial coordination, biosensor, DNA sensing*

INTRODUCTION

As an emerging molecular crystalline material, metal−organic frameworks (MOFs) process the unique characters associated with the large surface area, tunable pore scale, and good thermal stability.[1−3] In particular, MOF nanosheets, a novel kind of two-dimensional (2D) materials, have been extensively applied in catalysis,[4,5] biomimetic materials,[6,7] gas separation,[8] sensing,[9] and cancer therapy[10] because of their attractive ultrathin thickness structure.[11−13] The MOF nanosheet can be obtained from "top−down" methods[14−17] as well as "bottom−up" methods.[18−21] Oftentimes, extra substances are added to assist the formation of MOF nanosheets, causing the sealing of the metal site and thus obstructing its post-modification and application.[22−25] In contrast, Hofmann-type MOFs are a versatile class of materials with a $M^1[M^2(CN)_y]$ network, in which, the M^1 and M^2 metal ions are both transition metals with octahedral and square planar coordination, respectively.[26−31] The structure of Hofmann MOFs can be regulated by intermolecular interactions between the guest molecules and reactive metal sites in host MOFs.[32,33] Therefore, the inherent layers of Hofmann MOF have the potential to downsize to MOF nanosheets through modulation and exfoliation. Moreover, the exposed M^1 and M^2 metal ions of Hofmann MOF nanosheets own an exclusive axial coordination site with fluorophores for signal switching.

DNA detection with various optical and electronic techniques is an important approach in gene profiling and early diagnosis of cancer.[34−40] Many 2D nanomaterials are extensively involved in DNA detection because of their unique properties, such as large surface area, excellent optical transparency, and superior thermal stability.[41−46] These 2D nanomaterials as an efficient signal transduction platform usually quench the fluorescence of probes through fluorescence resonance energy transfer (FRET) or photo-induced electron-transfer pathway.[47−50] Alternatively, the ligand-to-metal charge transfer (LMCT) is an exclusive fluorescence-quenching approach for coordination compounds. That is, the electron of ligand excited by light can transfer to metal center, and then the metal excited state is back to the ground state through nonradiative relaxation.[51−55] On the basis of the unique $M^1[M^2(CN)_y]$ network, here, the Hofmann MOF nanosheets were utilized as an axial coordination platform for a new sight in signal switching through the LMCT quenching mechanism.

The inherent layers of Hofmann-type MOF have the potential to downsize to metal−organic layer through

Received: January 12, 2019
Accepted: March 12, 2019
Published: March 12, 2019

DOI: 10.1021/acsami.9b00693
ACS Appl. Mater. Interfaces 2019, 11, 12986−12992

modulation and exfoliation. In this work, to regulate the interaction between adjacent layers in MOF structures, two different types of rigid modulators, diethyl 4-pyridylphosphonate (4-PyP) and diethyl 3-pyridylphosphonate (3-PyP), were synthesized. Then, two different dimensional Hofmann MOFs, $[Fe(4\text{-}PyP)(H_2O)][Pt(CN)_4]\cdot H_2O\cdot CH_3OH$ (hMOF-1) and $[Fe(3\text{-}PyP)][Pt(CN)_4]$ (hMOF-2), were first prepared by modulating the positions of phosphonate in 4-PyP and 3-PyP isomer modulators. Significantly, hMOF-1 with twisty layers could be easily exfoliated to monolayer nanosheets by ultrasonic treatment. The monolayer nanosheets possessed excellent fluorescence-quenching ability through axial coordination between the fluorophores and Fe^{2+} ions of hMOF-1 nanosheets, providing a unique strategy for using Hofmann MOF monolayer nanosheets with open axial metal sites in DNA biosensing.

EXPERIMENTAL SECTION

Synthesis of Modulators Diethyl 4-Pyridylphosphonate (4-PyP) and Diethyl 3-Pyridylphosphonate (3-PyP). The 4-PyP and 3-PyP modulators were prepared according to the previous method (Figure S1).[56,57] Anhydrous toluene (50 mL) in a 100 mL three-necked round-bottom flask was bubbled with nitrogen for 30 min to remove oxygen. A mixture of bromopyridine hydrochloride (para- for 4-PyP/meta- for 3-PyP, 20 mmol), diethyl phosphite (24 mmol), and 8 mL of triethylamine was added into the flask under a nitrogen atmosphere. After heating up to 85 °C, tetrakis(triphenylphosphine) palladium (0.8 mmol) was added and the reaction temperature was maintained at 85 °C for 16 h. The white solids were filtered out, and the toluene solution was washed three times with deionized water (15 mL), dried over $MgSO_4$, and concentrated by distillation under reduced pressure. Silica gel chromatography eluting with a mixture of ethyl acetate and *n*-hexane (3:1, v/v) afforded diethyl pyridylphosphonate (4-PyP/3-PyP). Total yield: about 30.9% (4-PyP) and 43.5% (3-PyP). 4-PyP ^{1}H NMR ($CDCl_3$): δ 8.78 (t, 2H, J = 4.9 Hz), 7.67 (dd, 2H, J = 5.3, 13.3 Hz), 4.16 (m, 4H), 1.35 (t, 6H, J = 7.0 Hz). 3-PyP ^{1}H NMR ($CDCl_3$): δ 8.99 (d, J = 6.1 Hz, 1H), 8.79 (m, 1H), 8.12 (ddt, J = 7.7, 1.8, 13.2 Hz, 1H), 7.47 (m, 1H), 4.16 (m, 4H), 1.35 (t, 6H). m/z: 216 was represented 4-PyP and 3-PyP combined one proton (Figures S2 and S3).

Synthesis of Single-Crystal hMOF-1 and hMOF-2. The crystals were grown by the liquid diffusion method at room temperature because of the fast reaction rate between $Fe(ClO_4)_2\cdot 6H_2O$ and $K_2Pt(CN)_4\cdot 3H_2O$. Methanol, distilled water, and their mixed solution (1:1, v/v) were bubbled with nitrogen 30 min to remove oxygen. $Fe(ClO_4)_2\cdot 6H_2O$ (7.2 mg, 0.02 mmol) and the corresponding modulator (4-PyP or 3-PyP, 8.6 mg, 0.04 mmol) were added to 0.5 mL of methanol. Also, $K_2Pt(CN)_4\cdot 3H_2O$ (8.6 mg, 0.04 mmol) was dissolved in 0.5 mL distilled water. The 0.5 mL $K_2Pt(CN)_4$ water solution was placed at the bottom of a 5 mL tube first, and then, 4 mL of methanol/water was slowly added to the tube. After that, 0.5 mL of $Fe(4\text{-}PyP)_n$ or $Fe(3\text{-}PyP)_n$ methanol solution was slowly added to the tube too. Finally, nitrogen was also used to remove oxygen in tube and plastic wrap was used to seal the tube. The rhombus-shaped crystals were obtained after placing the tube steadily for 2 weeks.

Single-Crystal Structure Determination. Single crystals of hMOF-1 and hMOF-2 were selected for indexing and intensity data collection on a Bruker Smart Apex CCD diffractometer using graphite-monochromated Mo K_α radiation (λ = 0.71073 Å) at room temperature. The data were integrated using the Siemens SAINT program,[58] with the intensities corrected for Lorentz factor, polarization, air absorption, and absorption due to variation in the path length through the detector face plate. Absorption corrections were applied. The structures were solved by direct methods and refined on F^2 by full-matrix least squares using SHELXTL.[59] All of the nonhydrogen atoms were located from the Fourier maps and were refined anisotropically. All H atoms were refined isotropically with the isotropic vibration parameters related to the nonhydrogen atoms to which they are bonded.

Preparation of hMOF-1 Monolayer Nanosheet. hMOF-1 nanosheet dispersion was prepared via a conventional "top−down" approach. In a typical experiment, 1.0 mg of bulk hMOF-1 suspended in 2.5 mL water was subjected to ultrasonic treatment (SK3200KHC, 150 W, 53 kHz) for 60 min. The upper colloidal suspension of exfoliated hMOF-1 nanosheets was collected after sedimentation for 12 h and then used for characterization and fluorescent DNA detection.

Fluorescence DNA Detection. In a single DNA detection experiment, 10 μL of probe DNA (0.5 μM) and 10 μL of the target DNA (0−2 μM) were first hybridized in 220 μL of HEPES buffer (10 mM, pH 7.4) containing 100 mM Na^+ and 10 mM Mg^{2+} for about 10 min at 37 °C. After incubating with hMOF-1 nanosheet dispersion (10 μL, 0.4 mg mL^{-1}) for 10 min at room temperature, fluorescence measurements were used to monitor the detection process with the final concentration of target DNA (0−40 nM). The excitation and emission wavelengths were fixed at 490 and 516 nm, respectively. All reported fluorescence measurements were taken as an average of three replicates.

RESULTS AND DISCUSSION

Design and Structure Modulation of hMOF. The single crystals of hMOF-1 or hMOF-2 were grown by liquid diffusion of $Fe(ClO_4)_2\cdot 6H_2O$, $K_2Pt(CN)_4\cdot 3H_2O$ and 4-PyP or 3-PyP in water and methanol. Single-crystal X-ray diffraction revealed that hMOF-1 crystallized in the monoclinic system space group $P2_1/n$ with a zigzag 2D layered structure stacked as ABAB form while hMOF-2 crystallized in the monoclinic space group $P2_1/m$ with a 3D framework structure (Figures 1A and S4, Tables S1−S3). In hMOF-1, the $[Pt(CN)_4]^{2-}$ moiety and $Fe(H_2O)(4\text{-}PyP)$ moiety constituted a 2D layer extended in the ab plane (Figure 1B). As shown in Figure 1C, the oxygen atoms of coordinated water and nitrogen atoms of 4-PyP modulators occupied the axial sites of the octahedral Fe^{2+} ions,

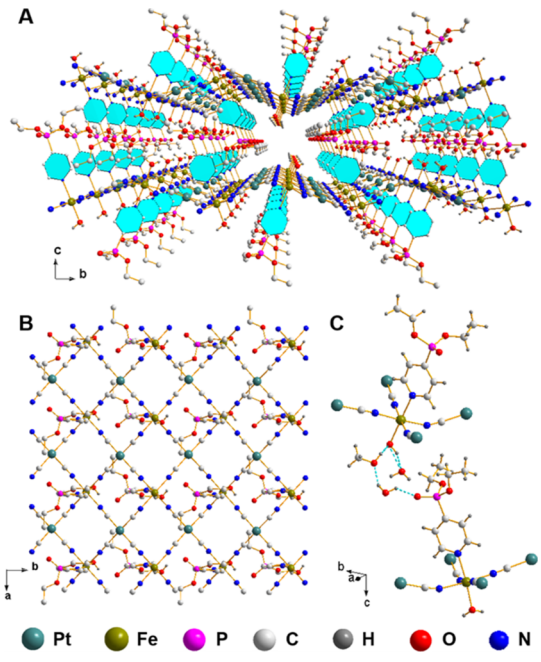

Figure 1. (A) Crystal structure of hMOF-1 and (B) its layer viewed along the *c*-axis. (C) Stacking interaction of two adjacent layers through H bonds in hMOF-1. Solvent molecules and H atoms are omitted except for coordinated water molecule in (A,B).

DOI: 10.1021/acsami.9b00693
ACS Appl. Mater. Interfaces 2019, 11, 12986−12992

and thus the 2D layers were cross-linked via H bonds among 4-PyP, the lattice solvents, and the coordinated water molecules.

On the other hand, the apical sites of Fe^{2+} ions in hMOF-2 were coordinated by the nitrogen atom and oxygen atom of two disordered 3-PyP modulators, thus leading to a 3D framework structure (Figure S4). The powder XRD (PXRD) patterns of hMOF-1 and hMOF-2 were consistent with the simulated patterns of the corresponding crystal samples (Figure S5). Moreover, the hMOFs demonstrated the characteristic infrared absorption peaks of phosphonate and cyano appeared at around 1000, 1200, and 2150 cm^{-1} (Figure S6A). The thermogravimetric analysis showed that hMOF-1 was decomposed at 180 °C while hMOF-2 at 300 °C, which is more unstable than hMOF-2 (Figure S6B). In a word, the two different dimension Hofmann MOFs' structures were successfully achieved by modulating the position of phosphonate groups of rigid ligands.

Characterization of hMOF-1 Monolayer Nanosheets. For both 4-PyP and 3-PyP ligands, the inherit layers of Hofmann MOFs showed Fe···Fe = 7.6 ± 0.1 Å and Pt···Pt = 7.1 ± 0.1 Å in $Fe[Pt(CN)_4]$ layers (Figures 1B and S4B). However, the adjacent layers of hMOF-1 and hMOF-2 were 12.6 and ∼9.0 Å (Figure 2), respectively, because the angle

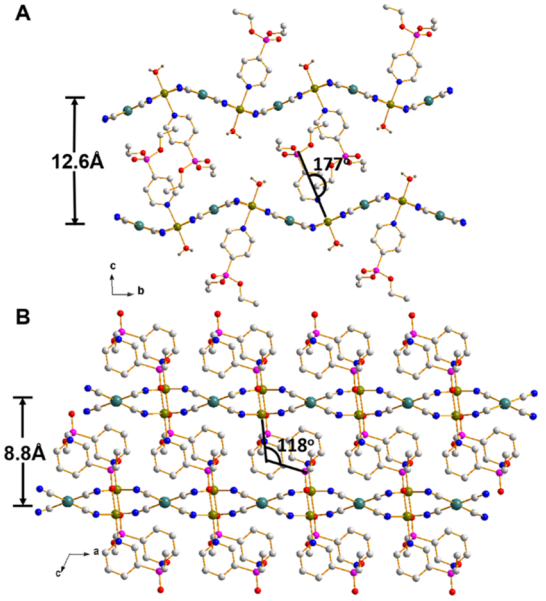

Figure 2. Distance between two adjacent layers and the angle between pyridine and phosphate group in modulators of hMOF-1 (A) and hMOF-2 (B).

between a pyridine and diethyl phosphate group in 4-PyP was closer to 180° than that in 3-PyP, which hindered the binding of the phosphonate oxygen atom with Fe^{2+} ions. Thus, the interactions among layers in hMOF-1 were weaker, and the layers could be separated easily. After ultrasonic treatment, the bulk hMOF-1 was simply exfoliated with the Tyndall effect through a conventional "top−down" method (Inset in Figure 3A). Transmission electron microscopy (TEM) showed the stacked hMOF-1 nanosheets with low contrast wrinkles and a lateral size of 300 nm (Figure 3A). In high-resolution TEM (HRTEM) image, hMOF-1 nanosheets showed a lattice pattern with an interplanar distance of 0.37 ± 0.01 nm (Figure 3C), which is consistent with the data (0.376 nm) for [200] plane of hMOF-1 in the PXRD pattern (Figure 3B). This

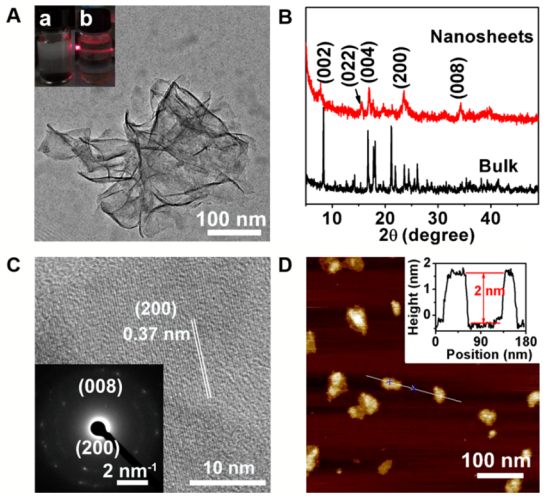

Figure 3. (A) TEM image of hMOF-1 nanosheets. Inset: Tyndall effect of the supernatant in water before (a) and after (b) ultrasonication. (B) PXRD patterns of hMOF-1 nanosheets (red) and bulk (black). (C) Lattice pattern in HRTEM image of hMOF-1 nanosheets. Inset: SAED image. (D) AFM height image of hMOF-1 nanosheets. Inset: Height profile along the white line.

result was also supported by the diffraction pattern of [200] in selected-area electron diffraction (Inset of Figure 3C). Meanwhile, the diffraction peaks to [008] could be contributed to the few-layer nanosheets. Furthermore, the bright field image of scanning TEM (STEM) and the energy-dispersive X-ray elemental mapping data exhibited a homogeneous distribution of metal ions on the whole hMOF-1 nanosheets, whereas secondary electron imaging showed an obvious lamellar surface (Figures S7 and S8). Atomic force microscopy (AFM) image demonstrated that the thickness of hMOF-1 nanosheets was 2.0 ± 0.2 nm (Figure 3D), which was also supported by the theoretical single-layer data (2.0 nm) from hMOF-1 single-crystal XRD patterns (Figure S9). The SEM image of bulk hMOF-1 and the sediment of hMOF-1 after sonication indicated the layer structure (Figure S10). In addition, the PXRD showed good stability of bulk hMOF-1, hMOF-1 nanosheets, and hMOF-2 (Figure S11). It is believed that phosphonate groups could weaken the interatomic force between two layers, so the layers could be separated easily under ultrasonic, resulting in the open metal site of MOF for axial coordination.

Quenching Mechanism of hMOF-1 Nanosheets. The quenching ability of hMOF-1 nanosheets was investigated by the 6-carboxyfluorescein labeled probe DNA (FAM-P) in various solvents. In HEPES, the quenching efficiency (QE) of hMOF-1 nanosheets for FAM-P (20 nM) was up to 91% in 10 min. However, the QEs were nearly down to 0% when the quenching process took place in PBS or Tris−HCl (Figure 4A). X-ray photoelectron spectroscopy (XPS) was used to recognize the interactions between Fe^{2+} sites of hMOF-1 nanosheets and fluorophores or solvents.[60] After being incubated with FAM-P, the Fe $2p_{3/2}$ and $2p_{1/2}$ peak positions at 711.2 and 724.6 eV for hMOF-1 nanosheets in HEPES shifted to 712.0 and 725.5 eV, respectively (Figure 4B), suggesting that the Fe^{2+} sites of hMOF-1 tended to interact with fluorophores. However, the interaction was blocked in PBS and Tris−HCl because of the occupation of phosphate and tris(hydroxymethyl)-aminomethane on the Fe^{2+} sites of nanosheets, respectively (Figure S12). Because there was no

DOI: 10.1021/acsami.9b00693
ACS Appl. Mater. Interfaces 2019, 11, 12986−12992

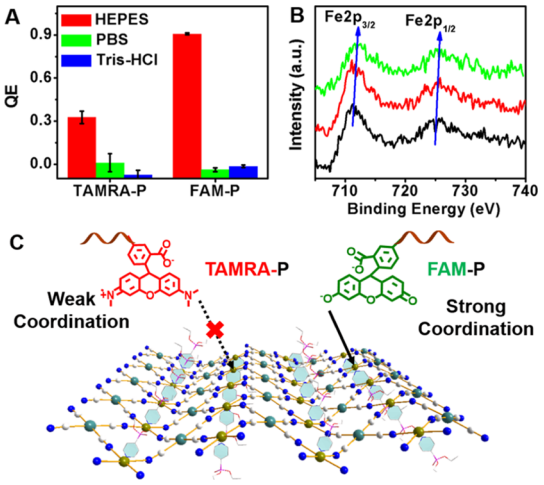

Figure 4. (A) QE of hMOF-1 nanosheets for 20 nM TAMRA-P or 20 nM FAM-P in HEPES, PBS and Tris−HCl. (B) Fe 2p XPS spectra of hMOF-1 nanosheets in HEPES before (black) and after being incubated with FAM-P (green) or TAMRA-P (red). (C) Axial coordination platform of hMOF-1 nanosheets for selective fluorescence quenching to FAM-P against TAMRA-P.

absorption at 400−800 nm in the UV−vis spectra (Figure S13), the quenching mechanism of hMOF-1 nanosheets was not realized via FRET but LMCT after the axial coordination between the Fe^{2+} sites of hMOF-1 nanosheets and fluorophore (Figure 4C).

Polyacrylamide gel electrophoresis (PAGE) of FAM-P, complementary target DNA (T), and their hybridization showed the individual electrophoresis distance (Figure 5A,

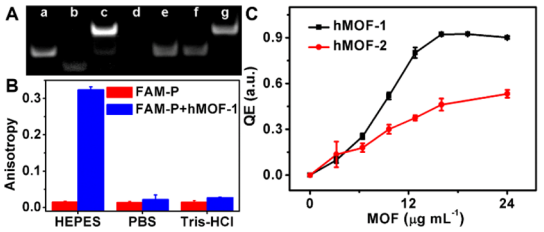

Figure 5. (A) PAGE image of 500 nM FAM-P (lane a), 500 nM T (lane b), mixture of 500 nM FAM-P and 500 nM T (lane c), 500 nM FAM-P + 80 μg mL^{-1} hMOF-1 nanosheets in HEPES (lane d), PBS (lane e), and Tris (lane f), and 500 nM FAM-P + 500 nM T + 80 μg mL^{-1} hMOF-1 nanosheets in HEPES (lane g). (B) Fluorescence anisotropy of FAM-P in the absence and presence of hMOF-1 nanosheets in HEPES, PBS, and Tris−HCl. (C) QE of hMOF-1 nanosheets within 10 min and hMOF-2 within 30 min (0−24 μg mL^{-1}) in response to FAM-P (20 nM) in HEPES.

lane a−c). Because of the big size of nanosheets, the FAM-P could not pass though the gel after strongly interacted with nanosheets in HEPES (lane d), but the bands for FAM-P still appeared in PBS and Tris−HCl (land e,f). On hybridization of FAM-P and T, the band for FAM-P/T duplex could be observed even in HEPES because of weak interaction between nanosheets and duplex (land g). Fluorescence anisotropy was utilized to analyze the affinity difference of hMOF-1 nanosheets toward FAM-P (Figure 5B). The anisotropies of FAM-P in all solvents were about 0.02, whereas the anisotropy of FAM-P in the presence of nanosheets was 0.32 in HEPES rather than 0.02 in PBS and Tris−HCl. Therefore, both PAGE and fluorescence anisotropy identified strong interactions between the FAM-P and hMOF-1 nanosheets in HEPES and weak interactions in PBS and Tris−HCl. As a comparison, 5-carboxytetramethylrhodamine (TAMRA), which had a similar main structure as FAM but different terminal tertiary amino groups, was employed to label probe DNA (TAMRA-P). The QE of hMOF-1 nanosheets for TAMRA-P was down to 30% in HEPES (Figure 4A), which should be attributed to the weak interactions between TAMRA and nanosheets (Figure 4B). In addition, hMOF-2 had similar composition but inherited a 3D structure that showed poor quenching ability (Figure 5C).

To prove the LMCT concept, the Lineweaver−Burk plot was carried out with a strong correlation between the concentration of hMOF-1 nanosheets and change of fluorescence intensity while Stern−Volmer plots denoted a weak correlation.[61] These phenomena indicated that the quenching process of hMOF-1 nanosheets followed static quenching rather than dynamic quenching (Figure S14). Moreover, FAM molecules could be quenched by hMOF-1 in a short time (Figure S15). More significantly, after being incubated with hMOF-1 nanosheets, the lifetime of FAM-P in HEPES decreased from 4.29 to 2.75 ns (Figures S16 and S17), which could be attributed to that the excited π^* electron of ligand transferred to d orbital of metal and then back to the ground state.[52,62] Therefore, LMCT fluorescence quenching was realized for the first time on 2D materials through axial coordination.

Furthermore, the LMCT process was identified in a mixture of PBS and HEPES. Because the phosphate could quickly replace water and thus hinder the contact of FAM-P and TAMRA-P with the nanosheets, the QE reduced to around 0% after 2 μM PBS was added (Figure 6A). The quenching

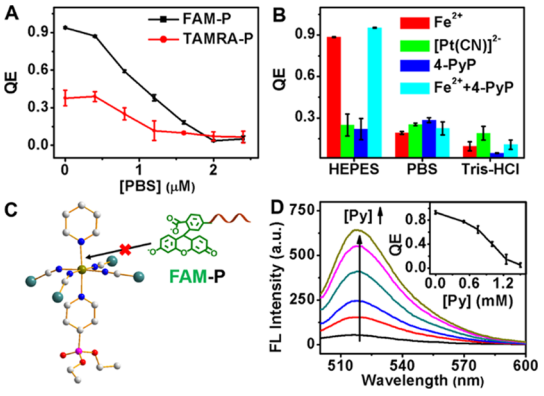

Figure 6. (A) QE of hMOF-1 nanosheets for FAM-P (20 nM) and TAMRA-P (20 nM) in 10 mM HEPES containing different concentrations of PBS. (B) QE of 100 μM Fe^{2+}, $[Pt(CN)_4]^{2-}$, 4-PyP, and mixture of Fe^{2+} and 4-PyP to 20 nM FAM-P in HEPES, PBS, and Tris−HCl. (C) Competitive axial coordination of hMOF-1 nanosheets and (D) Fluorescence-quenching efficiencies to pyridine concentrations against FAM-P.

behaviors of hMOF-1's individual components were also investigated (Figure 6B). $[Pt(CN)_4]^{2-}$ and 4-PyP could only quench no more than 30% fluorescence of FAM-P in all solvents. Meanwhile, Fe^{2+} and a mixture of Fe^{2+} and 4-PyP showed excellent quenching ability (over 90%) in HEPES but poor quenching ability (about 30%) in PBS and Tris−HCl. These results suggested that the Fe^{2+} played an important role in the quenching procedure. Moreover, pyridine-derived hMOF-1 nanosheets (hMOF-1-py) were used to study the

DOI: 10.1021/acsami.9b00693
ACS Appl. Mater. Interfaces 2019, 11, 12986−12992

effect of coordinated modulators. Because the axial site of hMOF-1 would be blocked by pyridine (Figure 6C), the quenching ability of the nanosheets was gradually suppressed with increasing concentrations of pyridine (Figure 6D). The above experiments indicated that the quenching mechanism of hMOF-1 nanosheets was dominated through LMCT between fluorophores and the Fe^{2+} sites of nanosheets, which demonstrated excellent quenching ability for FAM-DNA and showed great potential in biosensing.

Biosensing Application of hMOF-1 Nanosheets. Upon the hybridization of a single-strand DNA probe with target DNA to form a duplex, the distance between the duplex and 2D nanomaterials increased and their interactions became weak. The fluorescence correspondingly increased with more duplex formation, which could provide quantitative detection of the target analyte (Figure 7A). The fluorescence intensity of

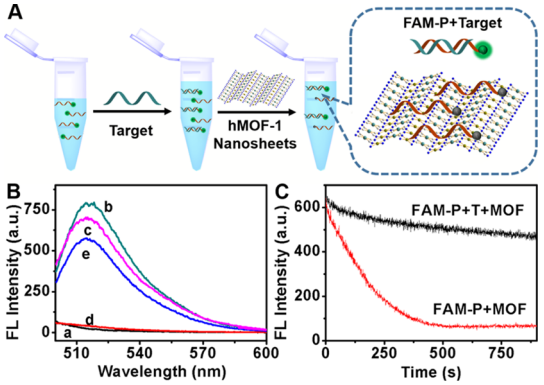

Figure 7. (A) Scheme illustration of hMOF-1 nanosheet-based axial coordination platform for DNA detection. (B) Fluorescence spectra of hMOF-1 nanosheets (a), 20 nM FAM-P (b,d), and 20 nM FAM-P/T1 duplex (c,e) in the absence (b,c) and presence (d,e) of hMOF-1 nanosheets. (C) Quenching dynamic curves of hMOF-1 nanosheets to 20 nM FAM-P and 20 nM FAM-P/T duplex.

double-strand DNA was about 9 times higher than that of FAM-P in the presence of hMOF-1 nanosheets (Figure 7B). On the basis of the excellent quenching capacity of hMOF-1 nanosheets (Figure 7C), the quantitative detection of T was achieved with a linear range from 1 to 40 nM (R^2 = 0.998) and the limit of detection of 0.3 nM (3σ). More importantly, hMOF-1 nanosheets displayed a good selectivity toward single-base mismatched DNA (Figure S18), providing promising applications in biosensing.

CONCLUSION

A Hofmann-type MOF material was precisely synthesized with 2D and 3D structures by modulating the position of phosphonate groups of rigid ligands. Because the direct binding between oxygen atom of phosphonate and Fe^{2+} ions was blocked by the diethyl group in 4-PyP, adjacent layers in hMOF-1 were linked via hydrogen bonds, which could make the hMOF-1 exfoliate easily to monolayers by classical "top–down" method. More significantly, hMOF-1 nanosheets as an axial coordination platform exhibited excellent quenching ability to fluorophores via a LMCT process that differed from the well-known FRET mechanism, leading to promising biosensing applications. This is the first report of using Hofmann MOF nanosheets as an axial coordination platform for signal switching. These results not only provide a novel quenching mechanism but also open a new window toward further applications of 2D MOF materials in biosensing in vitro and in vivo.

ASSOCIATED CONTENT

Supporting Information

The Supporting Information is available free of charge on the ACS Publications website at DOI: 10.1021/acsami.9b00693.

Detailed experiments, synthesis and characterization of modulators, crystal structure of hMOF-2, characterization and stability of bulk hMOF-1, hMOF-1 nanosheets and hMOF-2, interaction between hMOF-1 nanosheets and buffer, quenching mechanism of hMOF-1 nanosheets, fluorescence lifetime, calibration curve and selectivity of biosensor, and crystal parameters of hMOF-1 and hMOF-2 (PDF)

AUTHOR INFORMATION

Corresponding Authors

*E-mail: lmzheng@nju.edu.cn. Phone/Fax: +86-25-89681922 (L.Z.).

*E-mail: jpl@nju.edu.cn. Phone/Fax: +86-25-89689027 (J.L.).

ORCID

Li-Min Zheng: 0000-0003-4437-1105

Jianping Lei: 0000-0002-3594-180X

Author Contributions

All authors have given approval to the final version of the manuscript.

Notes

The authors declare no competing financial interest.

ACKNOWLEDGMENTS

This work was financially supported by the National Natural Science Foundation of China (21675084, 21605082, 21731003).

REFERENCES

(1) Liu, Y.; O'Keeffe, M.; Treacy, M. M. J.; Yaghi, O. M. The Geometry of Periodic Knots, Polycatenanes and Weaving from a Chemical Perspective: A Library for Reticular Chemistry. *Chem. Soc. Rev.* **2018**, *47*, 4642–4664.

(2) Furukawa, H.; Cordova, K. E.; O'Keeffe, M.; Yaghi, O. M. The Chemistry and Applications of Metal-Organic Frameworks. *Science* **2013**, *341*, 1230444.

(3) Wang, Y.; Liu, Q.; Zhang, Q.; Peng, B.; Deng, H. Molecular Vise Approach to Create Metal-Binding Sites in MOFs and Detection of Biomarkers. *Angew. Chem., Int. Ed.* **2018**, *57*, 7120–7125.

(4) Cai, Z.-S.; Shi, Y.; Bao, S.-S.; Shen, Y.; Xia, X.-H.; Zheng, L.-M. Bioinspired Engineering of Cobalt-Phosphonate Nanosheets for Robust Hydrogen Evolution Reaction. *ACS Catal.* **2018**, *8*, 3895–3902.

(5) Ji, P.; Manna, K.; Lin, Z.; Feng, X.; Urban, A.; Song, Y.; Lin, W. Single-Site Cobalt Catalysts at New $Zr_{12}(\mu_3\text{-}O)_8(\mu_3\text{-}OH)_8(\mu_2\text{-}OH)_6$ Metal–Organic Framework Nodes for Highly Active Hydrogenation of Nitroarenes, Nitriles, and Isocyanides. *J. Am. Chem. Soc.* **2017**, *139*, 7004–7011.

(6) Huang, Y.; Zhao, M.; Han, S.; Lai, Z.; Yang, J.; Tan, C.; Ma, Q.; Lu, Q.; Chen, J.; Zhang, X.; Zhang, Z.; Li, B.; Chen, B.; Zong, Y.; Zhang, H. Growth of Au Nanoparticles on 2D Metalloporphyrinic Metal–Organic Framework Nanosheets Used as Biomimetic Catalysts for Cascade Reactions. *Adv. Mater.* **2017**, *29*, 1700102.

(7) Wang, Y.; Zhao, M.; Ping, J.; Chen, B.; Cao, X.; Huang, Y.; Tan, C.; Ma, Q.; Wu, S.; Yu, Y.; Lu, Q.; Chen, J.; Zhao, W.; Ying, Y.;

DOI: 10.1021/acsami.9b00693
ACS Appl. Mater. Interfaces 2019, 11, 12986–12992

Zhang, H. Bioinspired Design of Ultrathin 2D Bimetallic Metal-Organic-Framework Nanosheets Used as Biomimetic Enzymes. *Adv. Mater.* **2016**, *28*, 4149−4155.
(8) Peng, Y.; Li, Y.; Ban, Y.; Yang, W. Two-Dimensional Metal−Organic Framework Nanosheets for Membrane-Based Gas Separation. *Angew. Chem., Int. Ed.* **2017**, *56*, 9757−9761.
(9) Campbell, M. G.; Liu, S. F.; Swager, T. M.; Dincă, M. Chemiresistive Sensor Arrays from Conductive 2D Metal−Organic Frameworks. *J. Am. Chem. Soc.* **2015**, *137*, 13780−13783.
(10) Lan, G.; Ni, K.; Xu, R.; Lu, K.; Lin, Z.; Chan, C.; Lin, W. Nanoscale Metal−Organic Layers for Deeply Penetrating X-ray-Induced Photodynamic Therapy. *Angew. Chem., Int. Ed.* **2017**, *56*, 12102−12106.
(11) Xu, M.; Yuan, S.; Chen, X.-Y.; Chang, Y.-J.; Day, G.; Gu, Z.-Y.; Zhou, H.-C. Two-Dimensional Metal−Organic Framework Nanosheets as an Enzyme Inhibitor: Modulation of the α-Chymotrypsin Activity. *J. Am. Chem. Soc.* **2017**, *139*, 8312−8319.
(12) Zhao, M.; Huang, Y.; Peng, Y.; Huang, Z.; Ma, Q.; Zhang, H. Two-Dimensional Metal-Organic Framework Nanosheets: Synthesis and Applications. *Chem. Soc. Rev.* **2018**, *47*, 6267−6295.
(13) Zhao, M.; Lu, Q.; Ma, Q.; Zhang, H. Two-Dimensional Metal-Organic Framework Nanosheets. *Small Methods* **2017**, *1*, 1600030.
(14) Peng, Y.; Li, Y.; Ban, Y.; Jin, H.; Jiao, W.; Liu, X.; Yang, W. Metal-Organic Framework Nanosheets as Building Blocks for Molecular Sieving Membranes. *Science* **2014**, *346*, 1356−1359.
(15) Huang, J.; Li, Y.; Huang, R.-K.; He, C.-T.; Gong, L.; Hu, Q.; Wang, L.; Xu, Y.-T.; Tian, X.-Y.; Liu, S.-Y.; Ye, Z.-M.; Wang, F.; Zhou, D.-D.; Zhang, W.-X.; Zhang, J.-P. Electrochemical Exfoliation of Pillared-Layer Metal-Organic Framework to Boost the Oxygen Evolution Reaction. *Angew. Chem., Int. Ed.* **2018**, *57*, 4632−4636.
(16) Cliffe, M. J.; Castillo-Martínez, E.; Wu, Y.; Lee, J.; Forse, A. C.; Firth, F. C. N.; Moghadam, P. Z.; Fairen-Jimenez, D.; Gaultois, M. W.; Hill, J. A.; Magdysyuk, O. V.; Slater, B.; Goodwin, A. L.; Grey, C. P. Metal-Organic Nanosheets Formed via Defect-Mediated Transformation of a Hafnium Metal-Organic Framework. *J. Am. Chem. Soc.* **2017**, *139*, 5397−5404.
(17) Ding, Y.; Chen, Y.-P.; Zhang, X.; Chen, L.; Dong, Z.; Jiang, H.-L.; Xu, H.; Zhou, H.-C. Controlled Intercalation and Chemical Exfoliation of Layered Metal-Organic Frameworks Using a Chemically Labile Intercalating Agent. *J. Am. Chem. Soc.* **2017**, *139*, 9136−9139.
(18) Rodenas, T.; Luz, I.; Prieto, G.; Seoane, B.; Miro, H.; Corma, A.; Kapteijn, F.; Xamena, F. X. L.; Gascon, J. Metal-Organic Framework Nanosheets in Polymer Composite Materials for Gas Separation. *Nat. Mater.* **2015**, *14*, 48−55.
(19) Mei, X.; Ma, J.; Bai, X.; Zhang, X.; Zhang, S.; Liang, R.; Wei, M.; Evans, D. G.; Duan, X. A Bottom-Up Synthesis of Rare-Earth-Hydrotalcite Monolayer Nanosheets toward Multimode Imaging and Synergetic Therapy. *Chem. Sci.* **2018**, *9*, 5630−5639.
(20) Zhao, M.; Wang, Y.; Ma, Q.; Huang, Y.; Zhang, X.; Ping, J.; Zhang, Z.; Lu, Q.; Yu, Y.; Xu, H.; Zhao, Y.; Zhang, H. Ultrathin 2D Metal-Organic Framework Nanosheets. *Adv. Mater.* **2015**, *27*, 7372−7378.
(21) Makiura, R.; Motoyama, S.; Umemura, Y.; Yamanaka, H.; Sakata, O.; Kitagawa, H. Surface Nano-Architecture of a Metal-Organic Framework. *Nat. Mater.* **2010**, *9*, 565−571.
(22) Röder, R.; Preiß, T.; Hirschle, P.; Steinborn, B.; Zimpel, A.; Höhn, M.; Rädler, J. O.; Bein, T.; Wagner, E.; Wuttke, S.; Lächelt, U. Multifunctional Nanoparticles by Coordinative Self-Assembly of His-Tagged Units with Metal-Organic Frameworks. *J. Am. Chem. Soc.* **2017**, *139*, 2359−2368.
(23) Li, S.; Du, X.-S.; Li, B.; Wang, J.-Y.; Li, G.-P.; Gao, G.-G.; Zang, S.-Q. Atom-Precise Modification of Silver(I) Thiolate Cluster by Shell Ligand Substitution: A New Approach to Generation of Cluster Functionality and Chirality. *J. Am. Chem. Soc.* **2018**, *140*, 594−597.
(24) Ji, P.; Solomon, J. B.; Lin, Z.; Johnson, A.; Jordan, R. F.; Lin, W. Transformation of Metal-Organic Framework Secondary Building Units into Hexanuclear Zr-Alkyl Catalysts for Ethylene Polymerization. *J. Am. Chem. Soc.* **2017**, *139*, 11325−11328.
(25) Asha, K. S.; Bhattacharjee, R.; Mandal, S. Complete Transmetalation in a Metal-Organic Framework by Metal Ion Metathesis in a Single Crystal for Selective Sensing of Phosphate Ions in Aqueous Media. *Angew. Chem., Int. Ed.* **2016**, *55*, 11528−11532.
(26) Otsubo, K.; Haraguchi, T.; Kitagawa, H. Nanoscale Crystalline Architectures of Hofmann-type Metal-Organic Frameworks. *Coord. Chem. Rev.* **2017**, *346*, 123−138.
(27) Ni, Z.-P.; Liu, J.-L.; Hoque, M. N.; Liu, W.; Li, J.-Y.; Chen, Y.-C.; Tong, M.-L. Recent Advances in Guest Effects on Spin-Crossover Behavior in Hofmann-type Metal-Organic Frameworks. *Coord. Chem. Rev.* **2017**, *335*, 28−43.
(28) Pham, C. H.; Cirera, J.; Paesani, F. Molecular Mechanisms of Spin Crossover in the {Fe(pz)[Pt(CN)$_4$]} Metal-Organic Framework upon Water Adsorption. *J. Am. Chem. Soc.* **2016**, *138*, 6123−6126.
(29) Clements, J. E.; Price, J. R.; Neville, S. M.; Kepert, C. J. Hysteretic Four-Step Spin Crossover within a Three-Dimensional Porous Hofmann-like Material. *Angew. Chem., Int. Ed.* **2016**, *55*, 15105−15109.
(30) Gros, C. R.; Peprah, M. K.; Hosterman, B. D.; Brinzari, T. V.; Quintero, P. A.; Sendova, M.; Meisel, M. W.; Talham, D. R. Light-Induced Magnetization Changes in a Coordination Polymer Heterostructure of a Prussian Blue Analogue and a Hofmann-like Fe(II) Spin Crossover Compound. *J. Am. Chem. Soc.* **2014**, *136*, 9846−9849.
(31) Murphy, M. J.; Zenere, K. A.; Ragon, F.; Southon, P. D.; Kepert, C. J.; Neville, S. M. Guest Programmable Multistep Spin Crossover in a Porous 2-D Hofmann-Type Material. *J. Am. Chem. Soc.* **2017**, *139*, 1330−1335.
(32) Sakaida, S.; Otsubo, K.; Sakata, O.; Song, C.; Fujiwara, A.; Takata, M.; Kitagawa, H. Crystalline Coordination Framework Endowed with Dynamic Gate-Opening Behaviour by Being Downsized to a Thin Film. *Nat. Chem.* **2016**, *8*, 377−383.
(33) Haraguchi, T.; Otsubo, K.; Sakata, O.; Fujiwara, A.; Kitagawa, H. Guest-Induced Two-Way Structural Transformation in a Layered Metal-Organic Framework Thin Film. *J. Am. Chem. Soc.* **2016**, *138*, 16787−16793.
(34) Das, J.; Ivanov, I.; Montermini, L.; Rak, J.; Sargent, E. H.; Kelley, S. O. An Electrochemical Clamp Assay for Direct, Rapid Analysis of Circulating Nucleic Acids in Serum. *Nat. Chem.* **2015**, *7*, 569−575.
(35) Das, J.; Ivanov, I.; Sargent, E. H.; Kelley, S. O. DNA Clutch Probes for Circulating Tumor DNA Analysis. *J. Am. Chem. Soc.* **2016**, *138*, 11009−11016.
(36) Huber, F.; Lang, H. P.; Backmann, N.; Rimoldi, D.; Gerber, C. Direct Detection of a BRAF Mutation in Total RNA from Melanoma Cells Using Cantilever Arrays. *Nat. Nanotechnol.* **2013**, *8*, 125−129.
(37) Cecconello, A.; Besteiro, L. V.; Govorov, A. O.; Willner, I. Chiroplasmonic DNA-Based Nanostructures. *Nat. Rev. Mater.* **2017**, *2*, 17039.
(38) Zhu, L.; Zhou, J.; Xu, G.; Li, C.; Ling, P.; Liu, B.; Ju, H.; Lei, J. DNA Quadruplexes as Molecular Scaffolds for Controlled Assembly of Fluorogens with Aggregation-Induced Emission. *Chem. Sci.* **2018**, *9*, 2559−2566.
(39) Liu, X.; Wang, F.; Aizen, R.; Yehezkeli, O.; Willner, I. Graphene Oxide/Nucleic-Acid-Stabilized Silver Nanoclusters: Functional Hybrid Materials for Optical Aptamer Sensing and Multiplexed Analysis of Pathogenic DNAs. *J. Am. Chem. Soc.* **2013**, *135*, 11832−11839.
(40) Wang, F.; Liu, X.; Willner, I. DNA Switches: From Principles to Applications. *Angew. Chem., Int. Ed.* **2015**, *54*, 1098−1129.
(41) Lu, C.-H.; Yang, H.-H.; Zhu, C.-L.; Chen, X.; Chen, G.-N. A Graphene Platform for Sensing Biomolecules. *Angew. Chem., Int. Ed.* **2009**, *48*, 4785−4787.
(42) Zhu, C.; Zeng, Z.; Li, H.; Li, F.; Fan, C.; Zhang, H. Single-Layer MoS_2-Based Nanoprobes for Homogeneous Detection of Biomolecules. *J. Am. Chem. Soc.* **2013**, *135*, 5998−6001.
(43) Tan, C.; Yu, P.; Hu, Y.; Chen, J.; Huang, Y.; Cai, Y.; Luo, Z.; Li, B.; Lu, Q.; Wang, L.; Liu, Z.; Zhang, H. High-Yield Exfoliation of Ultrathin Two-Dimensional Ternary Chalcoganide Nanosheets for

DOI: 10.1021/acsami.9b00693
ACS Appl. Mater. Interfaces 2019, 11, 12986−12992

Highly Sensitive and Selective Fluorescence DNA Sensors. *J. Am. Chem. Soc.* **2015**, *137*, 10430−10436.
(44) Zhang, Y.; Zheng, B.; Zhu, C.; Zhang, X.; Tan, C.; Li, H.; Chen, B.; Yang, J.; Chen, J.; Huang, Y.; Wang, L.; Zhang, H. Single-Layer Transition Metal Dichalcogenide Nanosheet-Based Nanosensors for Rapid, Sensitive, and Multiplexed Detection of DNA. *Adv. Mater.* **2015**, *27*, 935−939.
(45) Peng, Y.; Huang, Y.; Zhu, Y.; Chen, B.; Wang, L.; Lai, Z.; Zhang, Z.; Zhao, M.; Tan, C.; Yang, N.; Shao, F.; Han, Y.; Zhang, H. Ultrathin Two-Dimensional Covalent Organic Framework Nanosheets: Preparation and Application in Highly Sensitive and Selective DNA Detection. *J. Am. Chem. Soc.* **2017**, *139*, 8698−8704.
(46) Yuan, S.; Feng, L.; Wang, K.; Pang, J.; Bosch, M.; Lollar, C.; Sun, Y.; Qin, J.; Yang, X.; Zhang, P.; Wang, Q.; Zou, L.; Zhang, Y.; Zhang, L.; Fang, Y.; Li, J.; Zhou, H.-C. Stable Metal-Organic Frameworks: Design, Synthesis, and Applications. *Adv. Mater.* **2018**, *30*, 1704303.
(47) Noh, T. H.; Lee, H.; Jang, J.; Jung, O.-S. Organization and Energy Transfer of Fused Aromatic Hydrocarbon Guests within Anion-Confining Nanochannel MOFs. *Angew. Chem., Int. Ed.* **2015**, *54*, 9284−9288.
(48) Suresh, V. M.; George, S. J.; Maji, T. K. MOF Nano-Vesicles and Toroids: Self-Assembled Porous Soft-Hybrids for Light Harvesting. *Adv. Funct. Mater.* **2013**, *23*, 5585−5590.
(49) Zhu, X.; Zheng, H.; Wei, X.; Lin, Z.; Guo, L.; Qiu, B.; Chen, G. Metal-Organic Framework (MOF): a Novel Sensing Platform for Biomolecules. *Chem. Commun.* **2013**, *49*, 1276−1278.
(50) Gao, R.; Yan, D. Layered Host−Guest Long-Afterglow Ultrathin Nanosheets: High-Efficiency Phosphorescence Energy Transfer at 2D Confined Interface. *Chem. Sci.* **2017**, *8*, 590−599.
(51) Holbrook, R. J.; Weinberg, D. J.; Peterson, M. D.; Weiss, E. A.; Meade, T. J. Light-Activated Protein Inhibition through Photoinduced Electron Transfer of a Ruthenium(II)−Cobalt(III) Bimetallic Complex. *J. Am. Chem. Soc.* **2015**, *137*, 3379−3385.
(52) Ryland, E. S.; Lin, M.-F.; Verkamp, M. A.; Zhang, K.; Benke, K.; Carlson, M.; Vura-Weis, J. Tabletop Femtosecond M-edge X-ray Absorption Near-Edge Structure of FeTPPCl: Metalloporphyrin Photophysics from the Perspective of the Metal. *J. Am. Chem. Soc.* **2018**, *140*, 4691−4696.
(53) Fernández-Ariza, J.; Krick Calderón, R. M.; Rodríguez-Morgade, M. S.; Guldi, D. M.; Torres, T. Phthalocyanine−Perylenediimide Cart Wheels. *J. Am. Chem. Soc.* **2016**, *138*, 12963−12974.
(54) Lim, G. N.; Obondi, C. O.; D'Souza, F. A High-Energy Charge-Separated State of 1.70 eV from a High-Potential Donor−Acceptor Dyad: A Catalyst for Energy-Demanding Photochemical Reactions. *Angew. Chem., Int. Ed.* **2016**, *55*, 11517−11521.
(55) Hu, Z.; Deibert, B. J.; Li, J. Luminescent Metal-Organic Frameworks for Chemical Sensing and Explosive Detection. *Chem. Soc. Rev.* **2014**, *43*, 5815−5840.
(56) Ayyappan, P.; Evans, O. R.; Foxman, B. M.; Wheeler, K. A.; Warren, T. H.; Lin, W. New Open Frameworks Based on Metal Pyridylphosphonates. *Inorg. Chem.* **2001**, *40*, 5954−5961.
(57) Zon, J.; Videnova-Adrabinska, V.; Janczak, J.; Wilk, M.; Samoc, A.; Gancarz, R.; Samoc, M. Design, Synthesis and Noncentrosymmetric Solid State Organization of Three Novel Pyridylphosphonic Acids. *CrystEngComm* **2011**, *13*, 3474−3484.
(58) *SAINT, Program for Data Extraction and Reduction*; Siemens Analytical X-ray Instruments: Madison, WI, 1994−1996.
(59) *SHELXTL, Reference Manual; Siemens Industrial Automation* (version 5.0); Analytical Instruments: Madison, WI, 1995.
(60) Cao, R. G.; Thapa, R.; Kim, H.; Xu, X. D.; Kim, M. G.; Li, Q.; Park, N.; Liu, M. L.; Cho, J. Promotion of Oxygen Reduction by a Bio-Inspired Tethered Iron Phthalocyanine Carbon Nanotube-Based Catalyst. *Nat. Commun.* **2013**, *4*, 2076.
(61) Wang, Q.; Wang, W.; Lei, J.; Xu, N.; Gao, F.; Ju, H. Fluorescence Quenching of Carbon Nitride Nanosheet through Its Interaction with DNA for Versatile Fluorescence Sensing. *Anal. Chem.* **2013**, *85*, 12182−12188.
(62) Chorazy, S.; Zakrzewski, J. J.; Wang, J.; Ohkoshi, S.-i.; Sieklucka, B. Incorporation of Hexacyanidoferrate(III) Ion in Photoluminescent Trimetallic Eu(3-pyridone)$[Co_{1-x}Fe_x(CN)_6]$ Chains Exhibiting Tunable Visible Light Absorption and Emission properties. *CrystEngComm* **2018**, *20*, 5695−5706.

DOI: 10.1021/acsami.9b00693
ACS Appl. Mater. Interfaces 2019, 11, 12986−12992